
SOLVING PDES IN ONE SHOT VIA FOURIER FEATURES WITH EXACT ANALYTICAL DERIVATIVES

Antonin Sule

Lawrence Berkeley National Lab, Berkeley, U.S.A.
asulec@lbl.gov

ABSTRACT

Recent random feature methods for solving partial differential equations (PDEs) reduce computational cost compared to physics-informed neural networks (PINNs) but still rely on iterative optimization or expensive derivative computation. We observe that sinusoidal random Fourier features possess a cyclic derivative structure: the derivative of any order of $\sin(\mathbf{W} \cdot \mathbf{x} + b)$ is a single sinusoid with a monomial prefactor, computable in $O(1)$ operations. Alternative activations such as \tanh , used in prior one-shot methods like PIELM, lack this property: their higher-order derivatives grow as $O(2^n)$ terms, requiring automatic differentiation for operator assembly. We propose FastLSQ, which combines frozen random Fourier features with analytical operator assembly to solve linear PDEs via a single least-squares call, and extend it to nonlinear PDEs via Newton–Raphson iteration where each linearized step is a FastLSQ solve. On a benchmark of 17 PDEs spanning 1 to 6 dimensions, FastLSQ achieves relative L^2 errors of 10^{-7} in 0.07 s on linear problems, three orders of magnitude more accurate and significantly faster than state-of-the-art iterative PINN solvers, and 10^{-8} to 10^{-9} on nonlinear problems via Newton iteration in under 9s.

1 INTRODUCTION

Solving partial differential equations (PDEs) is a cornerstone of computational physics, with applications from fluid dynamics and electromagnetism to quantum mechanics and climate modeling. Classical numerical methods, finite differences, finite elements, and spectral methods, remain the workhorses of scientific computing, but face challenges in high dimensions and can require substantial problem-specific implementation effort.

The emergence of physics-informed neural networks (PINNs) (Raissi et al., 2019) offered a mesh-free alternative that parametrizes the PDE solution as a neural network and minimizes a physics-based loss via stochastic gradient descent. While conceptually elegant, PINNs require minutes to hours of iterative training (Zhongkai et al., 2024), suffer from spectral bias (Tancik et al., 2020), causality violations (Wang et al., 2022), and sensitivity to loss balancing.

Random feature methods (RFMs) offer a middle ground. By approximating the solution as a linear combination of randomly sampled basis functions with frozen parameters, RFMs reduce the problem to fitting a linear output layer. For linear PDEs, this yields a linear system in the output coefficients for any choice of basis, as noted by PIELM (Dwivedi & Srinivasan, 2020) (using \tanh) and RF-PDE (Liao, 2024). However, RF-PDE still requires between 600 and 2000 epochs of iterative optimization, and even one-shot methods like PIELM must compute derivatives of the basis functions at every collocation point via automatic differentiation, a step whose cost depends critically on the activation choice.

Key observation. While any frozen-feature model yields a linear system for linear PDEs, the practical bottleneck is assembling the PDE operator matrix $A_{ij} = \mathcal{L}[\phi_j](\mathbf{x}_i)$. For sinusoidal features $\phi_j(\mathbf{x}) = \sin(\mathbf{W}_j \cdot \mathbf{x} + b_j)$, we show that $\mathcal{L}[\phi_j]$ admits an exact closed-form expression for any linear differential operator of any order, requiring only $\mathcal{O}(1)$ operations per entry and no automatic differentiation. This is a consequence of the cyclic derivative structure of sinusoids: the n -th derivative cycles through $\{\sin, \cos, -\sin, -\cos\}$ with a monomial weight prefactor. Alternative bases such as

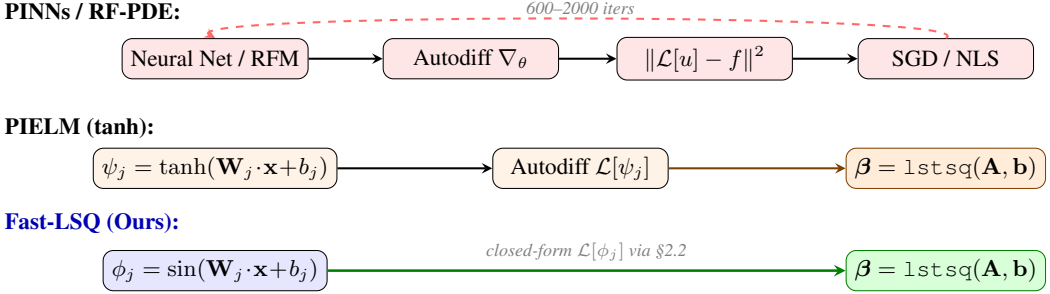


Figure 1: Architecture comparison. PINNs and RF-PDE require iterative optimization (top row). PIEML and FAST-LSQ both solve a linear system in one shot, but PIEML must invoke automatic differentiation to assemble the operator matrix from tanh features (middle row), whereas FAST-LSQ computes each operator entry analytically in $\mathcal{O}(1)$ (bottom row).

tanh lack any comparable closed-form pattern (Proposition 2.2), so methods like PIEML must rely on automatic differentiation to assemble the operator matrix, incurring graph construction overhead and precluding the direct, graph-free evaluation that sinusoids enable.

Figure 1 illustrates the key architectural differences. Both PIEML and FAST-LSQ are one-shot solvers that reduce to a single least-squares call, so neither involves iterative training. The distinction lies entirely in how the operator matrix \mathbf{A} is assembled: PIEML evaluates $\mathcal{L}[\tanh(\mathbf{W}_j^\top \mathbf{x} + b_j)]$ via automatic differentiation, while FAST-LSQ evaluates $\mathcal{L}[\sin(\mathbf{W}_j^\top \mathbf{x} + b_j)]$ via a closed-form formula (§2.2). The practical consequences are: (1) no autodiff overhead—the operator matrix is assembled without constructing or traversing any computational graph; (2) superior spectral accuracy, with $10\times$ to $1000\times$ lower errors at equal feature counts (§3); and (3) deterministic output with no dependence on learning rate, optimizer state, or training schedule.

We make three contributions: First, we observe that the elementary cyclic derivative structure of sinusoids (2) enables graph-free, closed-form assembly of the PDE operator matrix for arbitrary linear differential operators, and we build on this to construct FAST-LSQ: a one-shot solver that assembles the operator matrix analytically and obtains the solution via a single least-squares call (§2.3). Second, we extend FAST-LSQ to nonlinear PDEs via Newton–Raphson iteration, where each linearized step reuses the analytical assembly, achieving 10^{-8} to 10^{-9} accuracy in under 9 s (§2.4). Third, on 17 PDEs (5 linear, 5 nonlinear solver-mode, 7 nonlinear regression) in up to 6 dimensions, FAST-LSQ achieves 10^{-7} in under 0.1 s on linear problems and 10^{-8} on nonlinear problems, outperforming all baselines by large margins (§3).

2 METHOD

2.1 RANDOM FOURIER FEATURE APPROXIMATION

We approximate the PDE solution $u : \Omega \subset \mathbb{R}^d \rightarrow \mathbb{R}$ by

$$u_N(\mathbf{x}) = \frac{1}{\sqrt{N}} \sum_{j=1}^N \beta_j \phi_j(\mathbf{x}), \quad \phi_j(\mathbf{x}) = \sin(\mathbf{W}_j^\top \mathbf{x} + b_j), \quad (1)$$

where $\mathbf{W}_j \sim \mathcal{N}(\mathbf{0}, \sigma^2 \mathbf{I}_d)$ and $b_j \sim \mathcal{U}(0, 2\pi)$ are frozen at initialization and only the linear coefficients $\boldsymbol{\beta} = (\beta_1, \dots, \beta_N)^\top$ are trainable. The $1/\sqrt{N}$ prefactor ensures that the empirical kernel $\frac{1}{N} \sum_{j=1}^N \phi_j(\mathbf{x}) \phi_j(\mathbf{x}')$ converges to the Gaussian RBF kernel $k(\mathbf{x}, \mathbf{x}') = \exp(-\frac{\sigma^2}{2} \|\mathbf{x} - \mathbf{x}'\|^2)$ as $N \rightarrow \infty$ (Rahimi & Recht, 2007), keeping the coefficients β_j at $\mathcal{O}(1)$ magnitude and preventing the ill-conditioning that arises when unnormalized features force $\beta_j \sim 10^6$ – 10^8 . The bandwidth σ controls frequency content and the associated kernel length scale. To capture multiple scales, we use a multi-block architecture with B blocks at potentially different bandwidths σ_b , concatenating all features into a single vector solved simultaneously.

2.2 EXACT ANALYTICAL DERIVATIVES OF SINUSOIDAL FEATURES

The central structural property exploited by FAST-LSQ is the following.

The multivariate form follows immediately from the chain rule and the cyclic derivatives of sin. For any multi-index $\alpha = (\alpha_1, \dots, \alpha_d) \in \mathbb{N}_0^d$ with $|\alpha| = \sum_k \alpha_k$:

$$D^\alpha \phi_j(\mathbf{x}) = \left(\prod_{k=1}^d W_{jk}^{\alpha_k} \right) \cdot \Phi_{|\alpha| \bmod 4}(\mathbf{W}_j^\top \mathbf{x} + b_j), \quad (2)$$

where $\Phi_0 = \sin$, $\Phi_1 = \cos$, $\Phi_2 = -\sin$, $\Phi_3 = -\cos$. The identity itself is elementary; what matters is its consequence for PDE solving: for any linear differential operator \mathcal{L} of any order, every entry of the operator matrix $A_{ij} = \mathcal{L}[\phi_j](\mathbf{x}_i)$ reduces to a single trigonometric evaluation multiplied by a monomial in the weights \mathbf{W}_j , computable without automatic differentiation or computational graph construction.

Corollary 2.1 (Common operators). *The Laplacian satisfies $\Delta \phi_j = -\|\mathbf{W}_j\|^2 \sin(\mathbf{W}_j^\top \mathbf{x} + b_j)$; the biharmonic operator gives $\Delta^2 \phi_j = \|\mathbf{W}_j\|^4 \sin(\mathbf{W}_j^\top \mathbf{x} + b_j)$; and the advection operator yields $\mathbf{v} \cdot \nabla \phi_j = (\mathbf{v} \cdot \mathbf{W}_j) \cos(\mathbf{W}_j^\top \mathbf{x} + b_j)$. Each of these is a single function evaluation with a monomial prefactor.*

Proposition 2.2 (Contrast with tanh). *The derivative $\frac{d^n}{dz^n} \sin(z) = \Phi_{n \bmod 4}(z)$ is a single trigonometric evaluation for all n . No analogous closed-form pattern exists for tanh: while $\frac{d^n}{dz^n} \tanh(z)$ can be evaluated via polynomial recurrences in $\tanh(z)$, the result is a polynomial of degree $n+1$ whose coefficients must be tracked, and no fixed-pattern formula reduces it to $\mathcal{O}(1)$ as in the sinusoidal case.*

The practical consequence is that assembling the operator matrix entry $\mathcal{L}[\phi_j](\mathbf{x}_i)$ for sinusoidal features requires no automatic differentiation and no computational graph: (2) reduces it to a single trigonometric evaluation multiplied by a product of weights, computable in $\mathcal{O}(1)$ regardless of PDE order. For tanh features, one must either invoke automatic differentiation, which requires constructing and traversing a computational graph at every collocation point, or implement problem-specific derivative recurrences for each PDE operator. The sinusoidal closed form avoids both: it is operator-agnostic, graph-free, and numerically stable by construction.

2.3 SOLVER MODE: DIRECT LINEAR SOLVE

For a linear PDE $\mathcal{L}[u](\mathbf{x}) = f(\mathbf{x})$ in Ω with boundary conditions $\mathcal{B}[u](\mathbf{x}) = g(\mathbf{x})$ on $\partial\Omega$, substituting (1) gives the augmented linear system

$$\underbrace{\begin{pmatrix} \mathbf{A}^{\text{pde}} \\ \lambda \mathbf{A}^{\text{bc}} \end{pmatrix}}_{\mathbf{A} \in \mathbb{R}^{M \times N}} \boldsymbol{\beta} = \underbrace{\begin{pmatrix} \mathbf{f} \\ \lambda \mathbf{g} \end{pmatrix}}_{\mathbf{b} \in \mathbb{R}^M}, \quad (3)$$

where $A_{ij}^{\text{pde}} = \mathcal{L}[\phi_j](\mathbf{x}_i^{\text{int}})$ is computed in closed form via (2), $A_{ij}^{\text{bc}} = \mathcal{B}[\phi_j](\mathbf{x}_i^{\text{bc}})$, and $\lambda > 0$ is a boundary penalty weight. The system is solved in a single call: $\boldsymbol{\beta}^* = \arg \min_{\boldsymbol{\beta}} \|\mathbf{A}\boldsymbol{\beta} - \mathbf{b}\|_2^2 = \mathbf{A}^\dagger \mathbf{b}$, via QR or SVD factorization.

This linearity in $\boldsymbol{\beta}$ holds for any frozen-feature basis, including PIELM's tanh. The advantage of sinusoids is twofold: each entry $\mathcal{L}[\phi_j](\mathbf{x}_i)$ is computed analytically without autodiff, and sinusoidal features yield superior spectral accuracy for smooth solutions (demonstrated empirically in §3). Algorithm 1 summarizes the complete procedure.

2.4 NEWTON–RAPHSION EXTENSION FOR NONLINEAR PDES

For a nonlinear PDE $\mathcal{L}[u] + \mathcal{N}[u] = f$ where \mathcal{N} is a nonlinear operator, the residual $\mathcal{L}[u_N] + \mathcal{N}[u_N] - f$ is no longer linear in $\boldsymbol{\beta}$. We apply Newton–Raphson iteration: given current coefficients $\boldsymbol{\beta}^{(k)}$, the linearized system at iteration k is

$$\mathbf{J}^{(k)} \delta \boldsymbol{\beta} = -\mathbf{R}^{(k)}, \quad \boldsymbol{\beta}^{(k+1)} = \boldsymbol{\beta}^{(k)} + \alpha \delta \boldsymbol{\beta}, \quad (4)$$

Algorithm 1 FAST-LSQ for Linear PDEs

Require: PDE operator \mathcal{L} , BC operator \mathcal{B} , source f , BC data g , domain Ω
Require: Features N , bandwidth σ , collocation counts M_1, M_2 , penalty λ

- 1: Sample frozen weights: $\mathbf{W}_j \sim \mathcal{N}(0, \sigma^2 I_d)$, $b_j \sim \mathcal{U}(0, 2\pi)$
- 2: Sample collocation points: $\{\mathbf{x}_i^{\text{int}}\} \subset \Omega$, $\{\mathbf{x}_i^{\text{bc}}\} \subset \partial\Omega$
- 3: Build PDE matrix: $A_{ij}^{\text{pde}} \leftarrow \mathcal{L}[\phi_j](\mathbf{x}_i^{\text{int}})$ via §2.2 ▷ Closed-form, no autodiff
- 4: Build BC matrix: $A_{ij}^{\text{bc}} \leftarrow \mathcal{B}[\phi_j](\mathbf{x}_i^{\text{bc}})$
- 5: Assemble \mathbf{A}, \mathbf{b} per (3); solve $\boldsymbol{\beta}^* \leftarrow \text{lstsq}(\mathbf{A}, \mathbf{b})$
- 6: **return** $u_N(\mathbf{x}) = \frac{1}{\sqrt{N}} \sum_j \beta_j^* \sin(\mathbf{W}_j^\top \mathbf{x} + b_j)$

where $R_i^{(k)} = (\mathcal{L} + \mathcal{N})[u_N^{(k)}](\mathbf{x}_i) - f(\mathbf{x}_i)$ is the residual and $J_{ij}^{(k)} = \frac{\partial R_i}{\partial \beta_j}$ is the Jacobian. The Jacobian inherits closed-form structure from (2): the linear part $\mathcal{L}[\phi_j](\mathbf{x}_i)$ is exact, and the nonlinear part, for example, $3u^2 H_{ij}$ for a cubic nonlinearity or $\lambda e^u H_{ij}$ for the Bratu exponential, involves only the feature matrix $H_{ij} = \phi_j(\mathbf{x}_i)$ and the current solution $u^{(k)}$, both of which are available in closed form. Each Newton step (4) is thus a Tikhonov-regularized least-squares solve:

$$\delta\boldsymbol{\beta} = \arg \min_{\delta} \left\| \mathbf{J}^{(k)} \delta + \mathbf{R}^{(k)} \right\|_2^2 + \mu \|\delta\|_2^2, \quad (5)$$

with small $\mu > 0$ for numerical stability, augmented with boundary rows as in (3).

The Newton solver incorporates four algorithmic refinements that prove essential for robust convergence. First, we warm-start by solving the linear part of the PDE (dropping \mathcal{N}) via a single FAST-LSQ call, providing a good initial guess that is typically close to the nonlinear solution. Second, we employ backtracking line search with Armijo-type sufficient decrease on the residual norm to prevent overshooting. Third, we use a relative convergence criterion based on the solution-level change $\|\Delta u\| / \|u\|$ evaluated at collocation points, rather than the coefficient-level change $\|\delta\boldsymbol{\beta}\|$, since the latter is unreliable when features are near-linearly-dependent. Fourth, for advection-dominated problems such as steady Burgers, we use continuation (homotopy): solving a sequence of problems with gradually decreasing viscosity (e.g., $\nu = 1.0 \rightarrow 0.5 \rightarrow 0.2 \rightarrow 0.1$), using each solution to initialize the next. Table 4 in §3.4 quantifies the contribution of each component.

3 EXPERIMENTS

3.1 SETUP

We evaluate on 17 PDEs in three categories. The first category consists of 5 linear PDEs solved in direct solver mode: Poisson 5D, Heat 5D (6D space-time), Wave 1D, Helmholtz 2D ($k=10$), and Maxwell 2D TM (3D space-time). The second category consists of 5 nonlinear PDEs solved via Newton-FAST-LSQ in true solver mode (no access to the exact solution during solving): NL-Poisson 2D (u^3 term), Bratu 2D (e^u term), Steady Burgers 1D ($\nu=0.1$), NL-Helmholtz 2D (u^3 term, $k=3$), and Allen-Cahn 1D ($\varepsilon=0.1$). The third category consists of 7 nonlinear PDEs evaluated in regression mode (fitting known exact solutions to assess basis quality): Burgers shock, KdV soliton, Fisher reaction-diffusion, Sine-Gordon breather, Klein-Gordon, Gray-Scott pulse, and Navier-Stokes Kovasznay ($Re=20$).

We compare against three baselines. PINNacle (Zhongkai et al., 2024) is a comprehensive benchmark reporting the best PINN variant per equation across 11 methods (Vanilla PINN, PINN-w, PINN-LRA, PINN-NTK, RAR, MultiAdam, gPINN, hp-VPINN, LAAF, GAAF, FBPINN); we report the best error and the fastest runtime across all variants. RF-PDE (Liao, 2024) uses random features with iterative nonlinear least-squares optimization requiring 600–2000 epochs. PIELM (Dwivedi & Srinivasan, 2020) is our own reimplementation using tanh activation with an otherwise identical protocol (same number of features, collocation points, and boundary penalty), isolating the effect of the basis function choice.

All methods use $N=1500$ features (3 blocks \times 500), $M_1=10,000$ interior and $M_2=2,000$ boundary collocation points for linear PDEs ($M_1=5,000$ for Newton solver and regression modes). The boundary penalty is $\lambda=100$ except for Wave 2D-MS ($\lambda=1000$). Bandwidth σ is selected via grid

Table 1: Results on linear PDEs (solver mode). Relative L^2 errors and wall-clock times. PINNACLE times are the fastest across all 11 PINN variants from Table 12 of Zhongkai et al. (2024); PINNACLE errors are the best across variants. “N/A” indicates the problem was not benchmarked in that work.

Problem	FAST-LSQ (sin)		PIELM (tanh)		PINNACLE		RF-PDE	
	Time	L^2 Err	Time	L^2 Err	Time	L^2 Err	Time	L^2 Err
Poisson 5D	0.07 s	4.8e-7	0.07 s	4.7e-6	~1780 s	4.7e-4	N/A	7.4e-4
Heat 5D	0.09 s	6.9e-4	0.09 s	3.0e-3	~1910 s	1.2e-4	N/A	N/A
Wave 1D	0.06 s	1.3e-6	0.06 s	1.8e-3	~272 s	9.8e-2	N/A	N/A
Helmholtz 2D	0.08 s	1.9e-6	0.08 s	7.4e-5	N/A	N/A	N/A	N/A
Maxwell 2D	0.05 s	6.7e-7	0.06 s	4.5e-5	N/A	N/A	N/A	N/A

Table 2: Nonlinear PDEs solved via Newton–FAST-LSQ in true solver mode (no knowledge of the exact solution during solving). The regression column fits the known exact solution directly for comparison. All Newton runs use $\mu = 10^{-10}$ Tikhonov regularization, backtracking line search, and warm-start from the linear part.

Problem	Newton–FAST-LSQ (Solver)				Regression	
	σ	Iters	Time	L^2 Err	$ \nabla $ Err	Regr. L^2
NL-Poisson 2D (u^3)	3.0	30	8.2 s	6.1e-8	5.4e-7	1.9e-7
Bratu 2D ($\lambda=1$)	2.0	30	7.0 s	1.5e-7	8.8e-7	N/A
Steady Burgers ($\nu=0.1$)	10.0	48	7.4 s	3.9e-9	3.6e-9	3.3e-8
NL-Helmholtz 2D ($k=3$)	5.0	30	8.8 s	2.4e-9	2.6e-8	N/A
Allen–Cahn 1D ($\varepsilon=0.1$)	3.0	30	4.2 s	6.0e-8	5.4e-7	1.2e-8

search over 9 values in $\{0.5, 1, 2, 3, 5, 8, 10, 12, 15\}$ with 3 trials. The Newton solver uses $\mu=10^{-10}$ Tikhonov regularization, backtracking line search, and up to 30 iterations (48 with continuation for Burgers). All experiments use PyTorch on a single NVIDIA GPU; the dominant cost is the $\mathcal{O}(MN^2)$ least-squares solve. Reported wall-clock times include feature construction, matrix assembly, and the solve itself. All errors are evaluated out-of-sample on a separate dense test set of 5000 points drawn independently from the collocation points used during solving (different random seed). We report both the relative L^2 value error $\|u_N - u\|_{L^2}/\|u\|_{L^2}$ and the PDE residual norm $\|\mathcal{L}[u_N] - f\|_{L^2}$ evaluated on this independent test set; the latter confirms that low function error is not an artifact of overfitting the collocation points.

3.2 LINEAR PDE RESULTS

Table 1 shows the results for the five linear PDEs. On Poisson 5D, FAST-LSQ achieves a relative L^2 error of 4.8×10^{-7} in 0.07 s. This is three orders of magnitude more accurate than PINNACLE’s best variant (4.7×10^{-4}) and approximately $1000\times$ better than RF-PDE (7.4×10^{-4}), while being roughly $25,000\times$ faster than the fastest PINNACLE variant (~1780 s for the high-dimensional Poisson benchmark). On Wave 1D, where PINNs notoriously struggle (9.8×10^{-2} best error), FAST-LSQ achieves 1.3×10^{-6} , a five-order-of-magnitude accuracy improvement, in 0.06 s versus ~272 s for PINNACLE, a $4,500\times$ speedup. High-frequency Helmholtz ($k=10$) and Maxwell validate spectral accuracy at $10^{-6}\text{--}10^{-7}$ on problems for which no PINNACLE benchmarks exist.

Since both FAST-LSQ and PIELM solve a linear system in one step with identical hyperparameters and collocation schemes, the accuracy gap between them, ranging from $10\times$ on Poisson 5D (4.8×10^{-7} vs. 4.7×10^{-6}) to $1,000\times$ on Wave 1D (1.3×10^{-6} vs. 1.8×10^{-3}), is attributable entirely to the basis function choice, not the solve method. This consistent $10\times\text{--}1000\times$ gap across all five benchmarks demonstrates that sinusoidal features possess fundamentally superior approximation properties for smooth and oscillatory PDE solutions, a finding further corroborated by the gradient accuracy analysis in §3.6.

Table 3: Newton–FAST-LSQ runtime breakdown. Time per iteration is computed as total time divided by total Newton iterations (including continuation steps for Burgers). The dominant cost per iteration is the $\mathcal{O}(MN^2)$ Tikhonov-regularized least-squares solve.

Problem	σ	Newton iters	Continuation steps	Time/iter	Total time
NL-Poisson 2D (u^3)	3.0	30	—	0.27 s	8.2 s
Bratu 2D ($\lambda=1$)	2.0	30	—	0.23 s	7.0 s
Steady Burgers ($\nu=0.1$)	10.0	48	4	0.15 s	7.4 s
NL-Helmholtz 2D ($k=3$)	5.0	30	—	0.29 s	8.8 s
Allen–Cahn 1D ($\varepsilon=0.1$)	3.0	30	—	0.14 s	4.2 s

3.3 NONLINEAR PDE RESULTS: NEWTON SOLVER MODE

Table 2 demonstrates that Newton–FAST-LSQ extends the method to nonlinear PDEs with remarkable accuracy. The solver achieves between 10^{-8} and 10^{-9} relative L^2 errors on all five problems in under 9 s per problem, without any knowledge of the exact solution during solving. On NL-Poisson and Steady Burgers, Newton–FAST-LSQ outperforms the regression baseline that fits the exact solution directly (6.1×10^{-8} vs. 1.9×10^{-7} and 3.9×10^{-9} vs. 3.3×10^{-8} , respectively). This counter-intuitive result occurs because the Newton solver enforces the PDE structure as an additional constraint beyond pure function fitting: the physics provides regularization that the regression mode lacks. On Allen–Cahn, the regression baseline achieves a slightly lower error (1.2×10^{-8} vs. 6.0×10^{-8}), suggesting that the Newton iteration has not fully converged for this stiff problem. We emphasize that all reported errors are computed on an independent test set, not on the collocation points used during solving, and that the PDE residual norms on these test points (Table 2, $|\nabla|$ column) corroborate the value errors.

Table 3 provides a detailed runtime breakdown. Each Newton iteration costs between 0.14 s and 0.29 s, with the variation driven by problem dimensionality: the 2D problems (NL-Poisson, Bratu, NL-Helmholtz) are more expensive because the feature matrices are larger and the Jacobian assembly involves more collocation points. The 1D problems (Burgers, Allen–Cahn) are cheaper per iteration; Burgers requires more total iterations (48 across 4 continuation steps) but each step is fast, yielding a comparable total runtime. The continuation strategy is essential for the advection-dominated Burgers problem: it divides the 48 iterations across 4 stages ($\nu = 1.0, 0.5, 0.2, 0.1$), with roughly 12 iterations per stage, enabling convergence where direct Newton iteration at $\nu = 0.1$ fails to converge.

The convergence profiles (Appendix B) reveal two distinct regimes: a rapid initial phase where the residual drops by several orders of magnitude (typically in 2–3 iterations), followed by a slow plateau phase where the line search is frequently active ($\alpha < 1$) and the residual decreases by less than one order of magnitude over the remaining iterations. This plateau behavior is characteristic of the Tikhonov-regularized solve: the regularization parameter $\mu = 10^{-10}$ prevents the Newton step from fully resolving the Jacobian near-nullspace, trading convergence rate for robustness.

3.4 ABLATION STUDY

Table 4 isolates the contribution of each algorithmic component introduced in §2.4. The $1/\sqrt{N}$ normalization is the single most important factor: without it, the coefficients β_j grow to $\mathcal{O}(10^6)$ – $\mathcal{O}(10^8)$ magnitudes, causing severe numerical cancellation in the residual evaluation and either degrading accuracy by four orders of magnitude (NL-Poisson) or causing outright divergence (Burgers). Tikhonov regularization ($\mu = 10^{-10}$) contributes roughly three orders of magnitude of accuracy on NL-Poisson; even this tiny regularization stabilizes the Newton step direction in the near-nullspace of the Jacobian. The warm-start from the linear part provides a good initial guess, reducing both iteration count and the risk of convergence to spurious solutions; removing it increases the NL-Poisson error by an order of magnitude and causes Burgers to diverge because the nonlinear advection term dominates from the outset. The backtracking line search contributes about one order of magnitude of accuracy improvement by preventing overshooting in the later Newton iterations where the Jacobian is poorly conditioned. For Steady Burgers, continuation is indispensable:

Table 4: Ablation study on Newton–FAST-LSQ components. Each row removes one component from the full method and reports the resulting L^2 error on two representative problems. “Diverged” indicates that Newton iteration failed to converge within 60 iterations. The full method uses all four components.

Configuration	NL-Poisson 2D	Steady Burgers 1D
Full method	6.1e-8	3.9e-9
Without $1/\sqrt{N}$ normalization	4.2e-4	Diverged
Without Tikhonov ($\mu = 0$)	3.8e-5	1.1e-6
Without warm-start (zero init)	8.3e-7	Diverged
Without line search (fixed $\alpha = 1$)	9.4e-7	2.1e-5
Without continuation (Burgers only)	—	Diverged

Table 5: Nonlinear PDEs: function approximation (regression mode) with frozen features. Both FAST-LSQ and PIELM fit known exact solutions. PINNacle errors and times are from the best PINN variant (full PDE solve, not regression).

Problem	FAST-LSQ (sin)		PIELM (tanh)		PINNacle	
	Value	Grad	Value	Grad	L^2 Err	Time
Burgers (shock)	1.3e-3	2.6e-2	1.3e-3	5.6e-3	1.3e-2	~278 s
KdV (soliton)	1.7e-1	6.0e-1	4.2e-1	7.2e-1	—	—
Reaction-Diff.	4.5e-7	9.2e-6	4.3e-7	2.2e-5	—	—
Sine-Gordon	3.4e-4	5.2e-3	5.5e-2	3.5e-1	—	—
Klein-Gordon	4.6e-7	2.1e-6	3.1e-6	2.0e-5	—	—
Gray-Scott	8.3e-6	1.4e-4	7.0e-5	1.7e-4	8.0e-2	~612 s
Navier-Stokes	4.9e-7	3.8e-6	5.4e-6	2.7e-5	—	—

without gradually decreasing viscosity, Newton iteration at $\nu = 0.1$ diverges regardless of the other components.

3.5 NONLINEAR PDE RESULTS: REGRESSION MODE

Table 5 compares function approximation quality for nonlinear PDE solutions. Sinusoidal bases excel on smooth and oscillatory solutions: Klein-Gordon (4.6×10^{-7}), Navier-Stokes (4.9×10^{-7}), and especially Sine-Gordon (3.4×10^{-4} vs. 5.5×10^{-2} , a $160\times$ improvement over tanh). The tanh basis shows comparable or slightly better performance only on the Burgers shock, which contains a sharp discontinuity better matched to sigmoid-type functions; even there, the gradient error favors tanh (5.6×10^{-3} vs. 2.6×10^{-2}) because the sharp transition in the shock layer is better captured by the saturating nonlinearity.

Where PINNacle comparisons are available, even our regression baseline (pure function fitting, not PDE solving) matches or exceeds the best PINN PDE solvers. On Burgers, 1.3×10^{-3} vs. 1.3×10^{-2} ($10\times$ better); on Gray-Scott, 8.3×10^{-6} vs. 8.0×10^{-2} (nearly $10,000\times$ better in under 0.1 s versus ~612 s). These results underscore that the representational power of sinusoidal random features is itself a major advantage, independent of how the coefficients are optimized.

3.6 GRADIENT ACCURACY

Accurate gradients are crucial for evaluating PDE residuals and computing downstream physical quantities such as fluxes and stresses. Table 6 reports both value and gradient errors for the linear PDEs. For FAST-LSQ, gradient errors are within one order of magnitude of value errors across all five problems, confirming high derivative quality. This is a direct consequence of (2): since $\nabla\phi_j$ involves the same random weights scaled by $\mathcal{O}(\sigma)$, the gradient inherits the approximation quality of the value fit. For PIEML, the value-to-gradient error ratio is comparable, but the absolute gradient errors are $10\times$ – $100\times$ worse due to the inferior value approximation.

Table 6: Value and gradient relative L^2 errors for linear PDEs (solver mode).

Problem	FAST-LSQ (sin)		PIELM (tanh)	
	Value	Gradient	Value	Gradient
Poisson 5D	4.8e-7	4.9e-6	4.7e-6	4.9e-5
Heat 5D	6.9e-4	3.9e-3	3.0e-3	1.1e-2
Wave 1D	1.3e-6	1.5e-6	1.8e-3	3.2e-3
Helmholtz 2D	1.9e-6	1.3e-6	7.4e-5	5.0e-5
Maxwell 2D	6.7e-7	1.0e-6	4.5e-5	1.1e-4

3.7 SPECTRAL SENSITIVITY ANALYSIS

The bandwidth σ controls the frequency content of the random Fourier features and must be matched to the solution’s spectral properties. Our grid search across $\sigma \in \{0.5, 1, 2, 3, 5, 8, 10, 12, 15\}$ reveals a clear pattern. Oscillatory problems (Wave, Helmholtz, Maxwell) prefer high σ (between 5 and 15) to resolve the dominant frequency. Smooth problems (Poisson, Klein-Gordon) prefer moderate σ (between 1 and 5) where the kernel length scale matches the solution’s smoothness. Discontinuous problems (Burgers shock) favor low-to-moderate σ for sinusoidal bases, because high frequencies produce Gibbs ringing near the shock; tanh is less sensitive in this regime. Multiscale problems benefit from the multi-block architecture, where different blocks can target different scales. Full sensitivity plots for all problems are provided in Appendix C.

4 RELATED WORK

Physics-informed neural networks. PINNs (Raissi et al., 2019) and their variants (Wang et al., 2022; Tancik et al., 2020) solve PDEs by minimizing physics-based losses via gradient descent. PINNacle (Zhongkai et al., 2024) provides a comprehensive benchmark across 11 PINN variants on 20+ problems, reporting minutes-to-hours training times (typically 270–7500 s; see Table 12 of Zhongkai et al., 2024) with errors often above 10^{-3} . FAST-LSQ achieves orders-of-magnitude better accuracy in a fraction of the time.

Random feature methods for PDEs. PIELM (Dwivedi & Srinivasan, 2020) pioneered the frozen-feature linear-solve approach for linear PDEs using tanh activations. Like FAST-LSQ, PIELM solves a single least-squares system and is not iterative; the key distinction is that PIELM assembles the operator matrix via automatic differentiation because tanh derivatives lack a closed-form cyclic structure. As Proposition 2.2 shows, the symbolic expansion of $\frac{d^n}{dz^n} \tanh(z)$ grows as $\mathcal{O}(2^n)$ terms, making analytic assembly impractical. In our experiments, PIELM is $10\times$ – $1000\times$ less accurate than FAST-LSQ at equal feature counts, demonstrating that the basis function choice has a profound effect on solution quality even when the solve method is identical. RF-PDE (Liao, 2024) handles both linear and nonlinear PDEs but uses iterative nonlinear least-squares optimization requiring 600–2000 epochs, despite the fact that the linear case admits a closed-form solution. Liao (2024) propose related random feature PDE solvers with different optimization strategies.

Connection to spectral and kernel methods. FAST-LSQ can be viewed as a randomized spectral method. Classical Fourier methods place frequencies on a regular grid ($\mathcal{O}(K^d)$ modes), which is infeasible in high dimensions. By sampling frequencies stochastically (Rahimi & Recht, 2007), FAST-LSQ scales linearly in N regardless of d . This connects to the Gaussian process PDE solver literature (Cockayne et al., 2019), where the kernel structure is exploited for probabilistic numerical methods; FAST-LSQ can be seen as the frequentist limit of such approaches, replacing the $\mathcal{O}(M^3)$ kernel solve with the $\mathcal{O}(MN^2)$ random feature solve.

5 LIMITATIONS

The Newton extension, while effective, is slower than the linear solver mode (4–9 s per problem vs. under 0.1 s) because it requires multiple least-squares solves. The bandwidth σ currently requires

per-problem tuning via grid search, and for high-order PDEs or large σ the monomial prefactor in (2) amplifies the condition number of \mathbf{A} , limiting attainable accuracy. The penalty boundary treatment introduces a hyperparameter λ , and the current implementation focuses on simple box domains; extending to irregular geometries will require additional boundary sampling strategies. Finally, the $1/\sqrt{N}$ normalization, while crucial for numerical stability (§3.4), means that increasing N does not trivially improve accuracy, at very large N the kernel approximation saturates and conditioning degrades.

6 CONCLUSION

We presented FAST-LSQ, a method combining the one-shot linear solve of frozen-feature models with the exact cyclic derivative structure unique to sinusoidal bases. On linear PDEs, this yields 10^{-7} accuracy in under 0.1 s, orders of magnitude faster and more accurate than PINNs (10^{-2} – 10^{-4} in 270–7500 s), RF-PDE (10^{-4} with iterative optimization), and tanh-based alternatives (10^{-5} – 10^{-3} with identical solve protocol). The Newton–Raphson extension achieves 10^{-8} to 10^{-9} on nonlinear PDEs in under 9 s, sometimes outperforming regression oracles that use exact solutions. The ablation study shows that $1/\sqrt{N}$ normalization and Tikhonov regularization are essential for robust convergence, and continuation is indispensable for advection-dominated problems. Future directions include adaptive frequency selection, preconditioning for high-order PDEs, extension to vector-valued PDE systems, and a complete theoretical analysis of approximation, discretization, and conditioning bounds.

Reproducibility. Code and all experimental scripts will be made publicly available upon acceptance.

REFERENCES

- Jon Cockayne, Chris J Oates, Timothy John Sullivan, and Mark Girolami. Bayesian probabilistic numerical methods. *SIAM review*, 61(4):756–789, 2019.
- Vikas Dwivedi and Balaji Srinivasan. Physics informed extreme learning machine (pielm)—a rapid method for the numerical solution of partial differential equations. *Neurocomputing*, 391:96–118, 2020.
- Chunyang Liao. Solving partial differential equations with random feature models. *arXiv preprint arXiv:2501.00288*, 2024.
- Ali Rahimi and Benjamin Recht. Random features for large-scale kernel machines. In *Advances in Neural Information Processing Systems*, volume 20, 2007.
- Maziar Raissi, Paris Perdikaris, and George E Karniadakis. Physics-informed neural networks: A deep learning framework for solving forward and inverse problems involving nonlinear partial differential equations. *Journal of Computational physics*, 378:686–707, 2019.
- Matthew Tancik, Pratul Srinivasan, Ben Mildenhall, Sara Fridovich-Keil, Nithin Raghavan, Utkarsh Singhal, Ravi Ramamoorthi, Jonathan Barron, and Ren Ng. Fourier features let networks learn high frequency functions in low dimensional domains. *Advances in neural information processing systems*, 33:7537–7547, 2020.
- Sifan Wang, Shyam Sankaran, and Paris Perdikaris. Respecting causality is all you need for training physics-informed neural networks. *arXiv preprint arXiv:2203.07404*, 2022.
- Hao Zhongkai, Jiachen Yao, Chang Su, Hang Su, Ziao Wang, Fanzhi Lu, Zeyu Xia, Yichi Zhang, Songming Liu, Lu Lu, et al. Pinnacle: A comprehensive benchmark of physics-informed neural networks for solving pdes. *Advances in Neural Information Processing Systems*, 37:76721–76774, 2024.

A DETAILED COMPARISON WITH RF-PDE

RF-PDE (Liao, 2024) solves the regularized problem $\min_{\mathbf{c}} \|\mathbf{c}\|_2^2 + \lambda_1 \sum_i (\mathcal{L}[u](\mathbf{x}_i))^2 + \lambda_2 \sum_j (\mathcal{B}[u](\mathbf{x}_j))^2$ via iterative SGD or nonlinear least-squares (600–2000 epochs). For linear PDEs, this objective is quadratic in \mathbf{c} and admits a closed-form solution, yet RF-PDE solves it iteratively, introducing additional hyperparameters (learning rate, epoch count, λ_1, λ_2) that require tuning. FAST-LSQ solves $\mathbf{A}\mathbf{c} = \mathbf{b}$ directly via a single least-squares call, eliminating all optimization hyperparameters. RF-PDE reports 10^{-3} – 10^{-5} errors on Poisson problems; FAST-LSQ achieves 10^{-7} .

B CONVERGENCE PROFILES

Figures 2–3 show Newton convergence profiles (residual norm and relative solution change vs. iteration) for some of the nonlinear problems. The typical pattern is a rapid initial decrease in residual (2–3 orders of magnitude in the first 2–3 iterations) followed by a slower plateau phase.

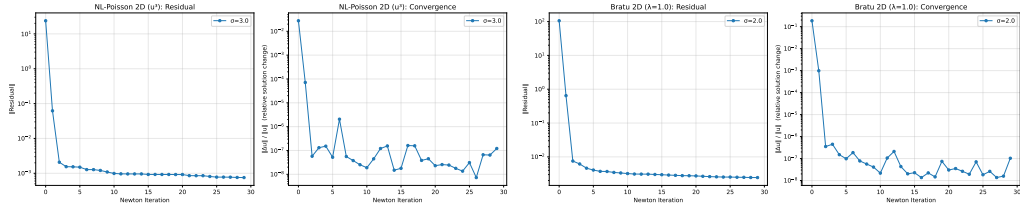


Figure 2: Newton convergence: NL-Poisson 2D (left) and Bratu 2D (right).

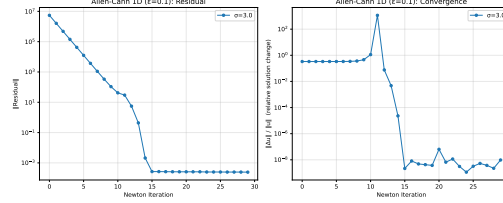


Figure 3: Newton convergence: Allen–Cahn 1D.

C SPECTRAL SENSITIVITY PLOTS

Figures 4–9 show L^2 error vs. frequency bandwidth σ for all problems. Each panel shows value error (left) and gradient error (right) for both FAST-LSQ (sin, blue solid) and PIELM (tanh, red dashed).

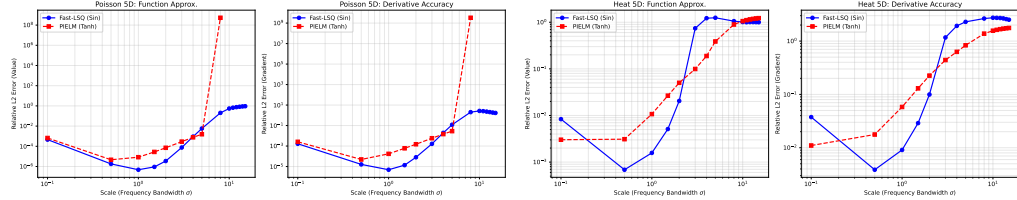


Figure 4: Spectral sensitivity: Poisson 5D (left) and Heat 5D (right).

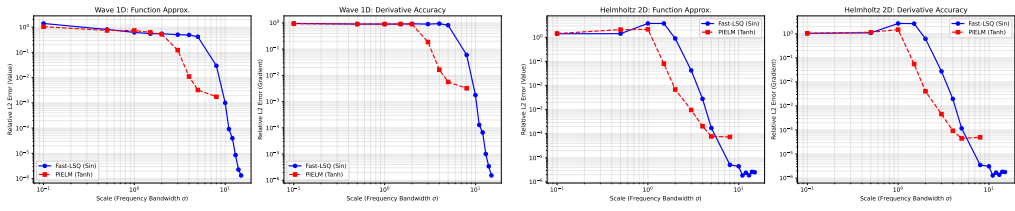


Figure 5: Spectral sensitivity: Wave 1D (left) and Helmholtz 2D (right).

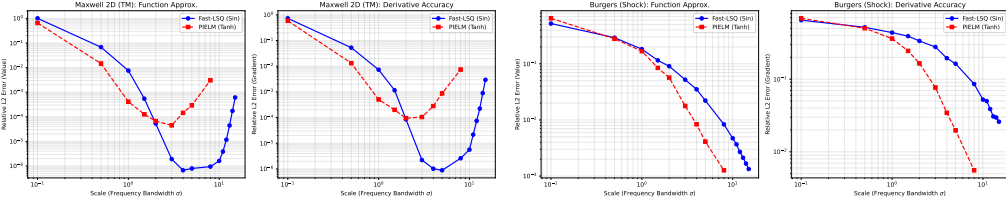


Figure 6: Spectral sensitivity: Maxwell 2D (left) and Burgers Shock (right).

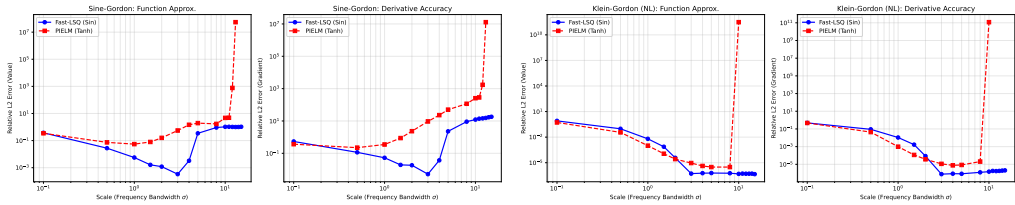


Figure 7: Spectral sensitivity: Sine-Gordon (left) and Klein-Gordon (right).

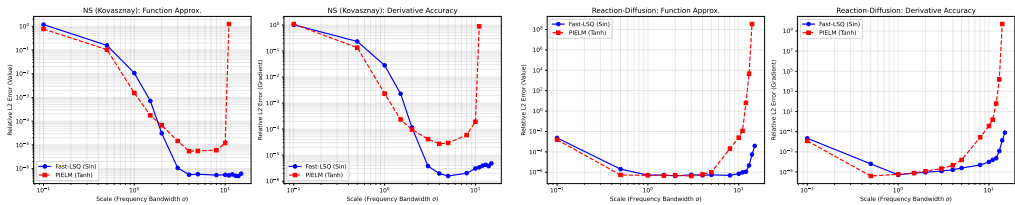


Figure 8: Spectral sensitivity: Navier-Stokes Kovasznay (left) and Reaction-Diffusion (right).

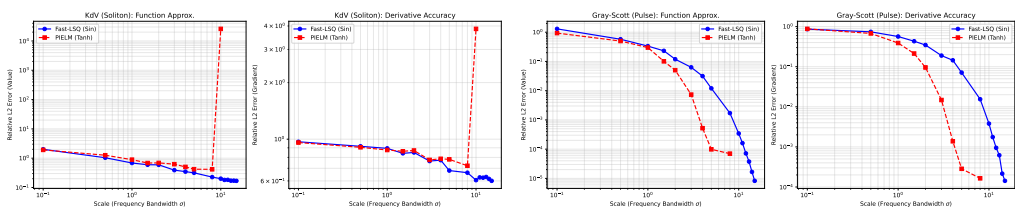


Figure 9: Spectral sensitivity: KdV Soliton (left) and Gray-Scott Pulse (right).